JOURNAL OF APPLIED ELECTROCHEMISTRY 22 (1992) 1147–1154

A hydrodynamic model for water decomposition in electrolyzers with a solid polymer electrolyte

A. B. GOLDBERG, L. I. KHEIFETS, A. G. VAGANOV,
S. G. OGRYZ'KO-ZHUKOVSKAYA, A. V. SHABALIN

State Research Institute of Chlorine, Moscow 109088, Russia

Received 3 May 1991; revised 16 March 1992

A new hydrodynamic model for two-phase water-electrolysis filtration in porous electrocatalysts and current collectors using a solid polymer electrolyte has been developed. The model takes into account the effect due to the internal structure of the porous elements on gas–liquid distribution and transport and electrochemical characteristics. Owing to the finite hydrodynamic permeability of porous elements, a limiting mass-exchange current was shown to set in, with the voltage tending to infinity because of the electrolyte depletion within the electrochemical reaction zone. The efficiency of the porous current collectors of various types has been considered under specified process conditions using computational modelling.

Nomenclature

C_0 water density (55.5×10^3 mol m^{-3})
d gas–liquid meniscus diameter, or pore diameter (m)
d_{bd} boundary pore diameter, model parameter (m)
F Faraday's constant (96 487 C mol^{-1})
H vapour pressure (Pa)
i reaction current density (A m^{-2})
i_0 exchange current density (A m^{-2})
J total current density (A m^{-2})
K effective permeability of porous layers (m^2)
K_m membrane hydraulic permeability (Pa^{-1} m s^{-1})
l porous layer thickness (m)
l_m membrane thickness (m)
N_0 membrane water-flow rate (mol m^{-2} s^{-1})
n membrane H_2O/H^+ molar flow ratio
P porous layer pressure (Pa)
P_{br} gas breakdown porous-layer pressure (Pa)
R gas constant (8.314 J mol^{-1} K^{-1})
S inner specific surface per unit volume of layer (m^{-1})
T temperature (K)
U cell voltage (V)
x coordinate for anodic part of cell (m)
y coordinate for cathodic part of cell (m)

Greek symbols
ε porosity (fraction of unity)
η dynamic viscosity (Pa s)
κ_0 solution conductivity within pores of reaction layer (Ω^{-1} m^{-1})
κ_m membrane conductivity (Ω^{-1} m^{-1})
μ electrochemical potential (J mol^{-1})
σ surface gas–liquid surface tension (N m^{-1})
ϕ surface overpotential for reaction (V)

Subscripts
g gas
l liquid
bd boundary
br gas breakdown
m membrane

Superscripts
a anode
c cathode

Indices
$i = 1$ catalytic layer
$i = 2$ current collector

1. Introduction

The necessity of a compromise between higher efficiency on the one hand and a smaller size on the other hand in the performance of an electrolyser has led to the wide use of solid polymer electrolytes (SPE®) supported on ion-exchange membranes (IEM). Electrodes for SPE® water electrolysis are fabricated from catalytically active noble metals (in pure form or as composites thereof) and are applied to the IEM surface as a porous layer with high adsorptive capacity [1]. The data available in this field of research are somewhat disparate and often controversial. For this reason, they are of little help in the practical design of commercial-sized SEP®-electrolysers with a potentially wide range of applications, from combinations with non-conventional sources of energy (solar cells, windmill generators) to their use in medicinal instrumentation. These difficulties are clearly indicative of the lack of a systematic approach to the study of SPE® water electrolysis, which is a difficult task considering the diversity of technological, constructional, and purely electrochemical factors involved in the performance of the electrolysers.

The aim of this work has been to develop a hydrodynamic model to explain major experimental effects

0021-891X

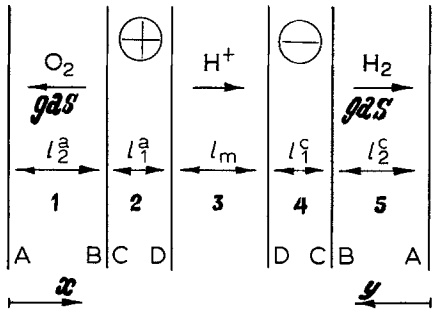

Fig. 1. Schematic diagram of a solid polymer electrolyte cell for water electrolysis.

observed in water electrolysis. Shown in Fig. 1 is the circuit of an electrochemical cell. The membrane (3) has porous catalyst layers (2, 4) applied to it. The supply of current and water is effected by means of a catalyst layer in contact with the porous collector (1, 5). The x-coordinate for the anodic part and the y-coordinate for the cathodic part of the cell are directed from the rear sides of the collector (at $x = 0$ and $y = 0$) toward the membrane. The letters A, B, C, and D in the diagram designate the boundary surfaces of the cell. The gases evolved are supposedly removed from the reaction zone through a network of large-sized pores within the porous layers and, analogously, the collectors. Thus, the volumetric 'gas-pore' structure (gas porosity) is dependent on the intrinsic porous layer properties and current density. It will be shown that the possible constraints imposed on the current density are associated with the increase in gas volume preventing the supply of water to the reaction zone. To avoid this problem, carefully balanced transport regimes within both the IEM and the collectors must be provided or, alternatively, an appropriate optimization of their structure is necessary. In view of these considerations, a hydrodynamic model must take into account the local dependence of filtration coefficients on gas content.

In the case of water supplied from the anodic part, the electrode reactions may be written as

$$\text{anode:}\quad (2 + x)H_2O \rightarrow O_2 + 4H^+(xH_2O) + 4e^-$$

$$\text{cathode:}\quad 4H^+(xH_2O) + 4e^- \rightarrow 2H_2 + xH_2O$$

In the anode process, the supply of water is somewhat in excess of stoichiometric because water molecules are carried over as constituents of the proton hydration shell to enter the cathode circuit as liquid droplets. Water for decomposition can also be fed in on the cathode side. In this case, water reaches the anode along the IEM pressure gradient almost stoichiometrically, and no liquid droplets are entrained in the water–oxygen gas mixture. Such a scheme for electrolysis is recommended if 'dry' oxygen is required.

The course of many mass-exchange limited electrochemical processes is, to a large extent, determined by hydrodynamic factors [2]. Most studies of the external mass exchange in IEM cells were carried out with the IEM in contact with a free electrolyte [3]. In this particular case of electrolysis we are concerned with porous bodies of essentially different structure exposed to electrolyte contact.

Earlier, Vol'fkovich *et al.* [4] studied the liquid–gas distribution in water electrolysis using a matrix-type SPE® cell similar to the present cell; however, these authors ignored the porous structure of the current collectors for cation and anion-exchange membranes as well as the effects arising from different schemes of water supply to the cell. The phase distribution inside the electrodes was presumed to be in thermodynamic equilibrium, and the pressure gradients confined within the IEM only. A hydrodynamic problem for the filtration of a liquid and a gas in electrodes as exemplified by the generation of chlorine from a chloride solution in a SPE® cell was considered in [5], with the object of developing a model for the diffusion-controlled transport of chloride ions into the reaction zone. For simplicity, the filtration coefficients for the gas and liquid phases were taken to be constant.

Here we distinguish three zones – membrane, electrode, and collector – in the hydrodynamic model. The gas–liquid interface is assumed to be confined within the pores, with their diameter defined by the Laplace capillary equilibrium condition. The compatibility of problem solutions in different zones has been defined in terms of the continuity of both mass fluxes and pressures in the phases corrected for a critical pressure ('breakdown' pressure) when a global mesh of gas pores is formed [6]. The analysis has been carried out in a quasihomogeneous approximation within the framework of a one-dimensional model.

2. Dynamic equations

To simplify the situation, it is assumed that the electrochemical reaction does not extend beyond a region close to the boundary D, that is, the reaction zone is essentially localized. This facilitates analysis of the hydrodynamic problem separately from the electrochemical, since the statement of the former problem does not require a knowledge of the strength of mass sources (either positive, or negative). Regrettably, no reliable information on the structure of active layers is available, and the above assumption is borne out, in a sense, by computations performed using different characteristic functions for the reaction distribution profile across the layer thickness. Thus, along with the point reaction source, a uniform reaction distribution across the entire layer has been considered, and a comparison of the results has not revealed any essential distinctions in hydrodynamic properties. By analogy with our previous work [5], the gas solubility will be ignored and Darcy's law is assumed to hold.

The model in question has provided a basis for computing the mass fluxes and voltage drop components in the electrolytic cell under specified conditions, viz temperature, pressure of generated gases, and steady-state current load.

We consider first the version with anodic supply of water (anode feed). Let J be the total current density

and N_0 the anode-to-cathode water flow rate across the membrane. Equations may be written for the pressure on the anode side in the liquid, P_l^a, in the gas, P_g^a; in the active layer ($i = 1$) and in the collector ($i = 2$). Thus,

$$\left.\begin{aligned} -\frac{K_{gi}^a}{\eta_g}\frac{H}{RT}\frac{dP_g^a}{dx} - \frac{K_{li}^a}{\eta_l}C_0\frac{dP_l^a}{dx} &= N_0 + \frac{J}{2F} \\ \frac{K_{gi}^a}{\eta_g}\frac{P_g^a - H}{RT}\frac{dP_g^a}{dx} &= \frac{J}{4F} \end{aligned}\right\} \quad (1)$$

In a similar manner, for the cathode side pressure for the liquid, P_l^c, and for the gas, P_g^c, is:

$$\left.\begin{aligned} -\frac{K_{gi}^c}{\eta_g}\frac{H}{RT}\frac{dP_g^c}{dy} - \frac{K_{li}^c}{\eta_l}C_0\frac{dP_l^c}{dy} &= -N_0 \\ \frac{K_{gi}^c}{\eta_g}\frac{P_g^c - H}{RT}\frac{dP_g^c}{dy} &= \frac{J}{2F} \end{aligned}\right\} \quad (2)$$

In each of the Systems, 1 and 2, the former equation expresses a constancy of the overall water flow rate, and the latter equation, constancy of the gas flow rate for oxygen and hydrogen. The temperature-dependent pressure for saturated vapour is designated by H. The permeabilities K_{gi}^a, K_{li}^a, K_{gi}^c, and K_{li}^c are dependent on the local moisture content and, consequently, are functions of the meniscus diameter d.

The Laplace capillary equation takes the form

$$P_g - P_l = \frac{4\sigma}{d} \quad (3)$$

The membrane water-flow rate includes electro-osmotic and hydraulic components and is expressed as

$$N_0 = n\frac{J}{F} + K_m c_0[P_l^a(D) - P_l^c(D)] \quad (4)$$

Hereafter, the bracketed letters A, B, C, and D will refer a particular quantity in question to the respective boundary as shown in Fig. 1. Equations 1, 3 and 4 with respect to P_g^a, P_l^a, and d^a, or Equations 2, 3 and 4 with respect to P_g^c, P_l^c, and d^c are to be solved simultaneously.

In formulating the boundary conditions, it is assumed that the pressures of the generated gases are known, that is the external pressures P^a and P^c and the gas breakdown pressures P_{br}^a, P_{br}^c ($i = 1, 2$) for the porous structures [6]. The set of boundary conditions takes the form:

(a) for continuity of the function of pressure in the liquid phase

$$\begin{aligned} P_l^a(A) &= P^a, \quad P_l^c(A) = P^c, \\ P_l^a(B) &= P_l^a(C), \quad P_l^c(B) = P_l^c(C) \end{aligned} \quad (5)$$

(b) for continuity of the function of pressure in the gas phase

$$P_g^a(A) = P^a + P_{br2}^a, \quad P_g^c(A) = P^c + P_{br2}^c \quad (6)$$

$$P_g^a(C) = \begin{cases} P_l^a(C) + P_{brl}^a & \text{at } P_g^a(B) - P_l^a(B) < P_{brl}^a \\ P_g^a(B) & \text{at } P_g^a(B) - P_l^a(B) \geqslant P_{brl}^a \end{cases} \quad (7)$$

$$P_g^c(C) = \begin{cases} P_l^c(C) + P_{brl}^c & \text{at } P_g^c(B) - P_l^c(B) < P_{brl}^c \\ P_g^c(B) & \text{at } P_g^c(B) - P_l^c(B) \geqslant P_{brl}^c \end{cases} \quad (8)$$

Conditions 6 are analogous to those as formulated for the infinite gas cluster which is formed during the extrusion of a liquid by a gas from a flooded porous body. However, in this particular case, Conditions 6 are valid only at the end-point of gas exit from the collector (point A). Otherwise stated, the hydraulic resistance for the exit of gas into the bulk of the liquid is assumed to be negligibly small in comparison to the hydraulic resistance across the collector. The same applies to Conditions 7 and 8, a distinction being that the gas, as produced by electrochemical reaction, is evolved from the catalytic layer not into liquid bulk, but rather into a porous collector. A situation may be envisaged when the pressure inside the collector is higher over P_{brl}, the condition which provides for continuity of pressure. This is exactly reflected in Inequalities 7 and 8.

In cathodic water supply (cathode feed), a significant pressure drop across the membrane may occur, which can offset the electroosmotic transfer and provide rather for water supply to the reaction zone D in the anode chamber. The decrease in pressure $P_l^a(D)$ will cause the meniscus diameter to diminish because of the easier filling of small-sized pores and the ensuing depletion of the anode region. The electrolytic oxygen should contain no gas-borne liquid, which, in fact, is observed in practice. The water flux across the membrane can then be accurately determined, since the total is composed of the reaction water and the water co-evaporated with oxygen:

$$N_0 = -\frac{J}{2F}\left(1 + \frac{1}{2}\frac{H}{P^a - H}\right) \quad (9)$$

Equations 2 hold for the cathode region subject to Boundary Conditions 5, 6 and 8. For the anode region, it may be assumed that $P_l^a(x) = P_l^a(D)$ throughout the entire range of $0 \leqslant x \leqslant l_1^a + l_2^a$, since no visible movement of liquid occurs, and the effect of evapocondensation on convection may be ignored. The latter of Equations 1 remains valid for the gas phase. Because of the water depletion in the anode region and the lack of suspended moisture in the free space of anodic circuit, the pressure P_g^a must be continuous at all the boundaries. To summarize briefly, a solution to the cathode-feed problem is as follows. By solving Equations 2, 3 and 9 the pressure $P_l^c(D)$ is found. Then, taking account of Equation 9, $P_l^a(D)$ is obtained from Equation 4, and further, $P_l^a(x) \equiv P_l^a(D)$. The latter of Equations 1, solved jointly with Equation 3, yields P_g^a.

Either of the two versions (cathode or anode feed) allow determination of the meniscus diameter, d, along with the phase pressure. Given the characteristics of the porous structure, a knowledge of d allows an estimation of the local moisture content and the specific liquid pore surface. These two quantities

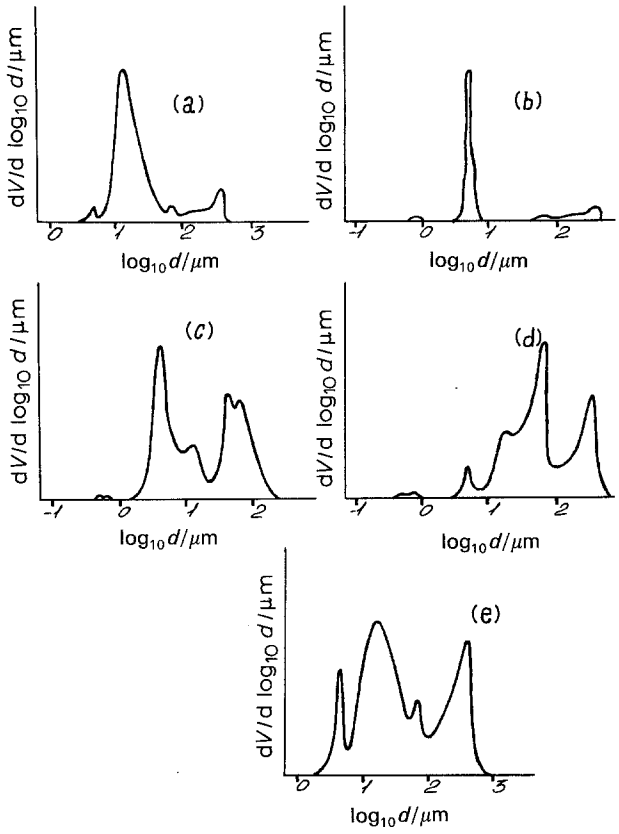

Fig. 2. Differential distribution curves (pore volume against diameter) for titanium current collectors: (a) Ti1; (b) Ti2; (c) Ti3; (d) Ti4; (e) Ti5. For convenience of comparison, the y-axis scale is normalized to a standard height of maximum intensity peaks.

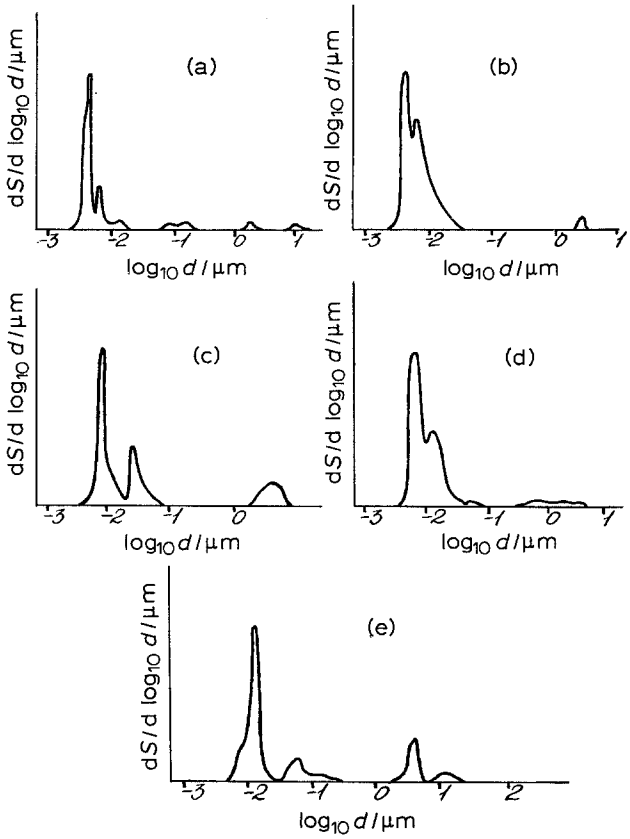

Fig. 3. Differential distribution curves (pore surface against diameter) for titanium current collectors: (a) Ti1; (b) Ti2; (c) Ti3; (d) Ti4; (e) Ti5 (y-axis scale normalized: see Fig. 2).

determine the transport and electrochemical properties of the system.

3. Properties of porous elements

Shown in Fig. 2 are differential curves for the pore volume against pore diameter distribution as measured on the porous titanium collectors used in the experiments. The differential curves for the pore surface versus pore diameter distribution are shown in Fig. 3. The porous structure parameters for the current collectors were measured by mercury porosimetry on an Autopore 9200 (Cultronix) instrument, with a computerized processing of the recorded measurements. Listed in Table 1 are the overall porosity, specific inner pore surface, mean pore diameter and gas breakdown pressure.

The porous materials typically exhibit a broad, mostly bimodal, distribution in macropore volume for pore diameters of about 1 μm and higher. Presumably, in a collector with perfect performance, the boundary between the diameters of gaseous and liquid pores corresponds roughly to the distance between the two neighbouring peaks in the curves. To determine the phase permeability coefficients, we have used the correlation in [7], which is known to hold for typical porous materials with a wide diameter distribution in the single-phase filtration regime. Its applicability to the separate filtration of gas and liquid phases requires special consideration and, ultimately, can be assessed from a standpoint of practical utility of the mathematical model chosen.

Let ε be the porosity of a collector; S, the inner specific surface and ρ/ρ_0 the ratio of the resistance of the electrolyte-filled collector to the resistance of the respective layer of free electrolyte. According to [7], the square of the hydraulic radius $m = \varepsilon/S$ and the hydraulic permeability coefficient K relate to each other as $m^2/K = (3.666 \pm 0.0988)\ (\rho/\rho_0)$ using the approximation $\rho_0/\rho = \varepsilon/3$ gives the relationship

$$K = \varepsilon^3/(11S^2) \qquad (10)$$

which agrees, within a constant factor, with the well-known Karman–Kozeny equation. As is seen in Figs 2 and 3, the macropores account for a larger part of the volume, and the mesopores, for most of the inner surface. Since the mesopores and micrometre-sized pores are spaced by a wide gap of 'forbidden' diameters, i.e. the intermediate pore diameters do not really come into play, it is assumed that the mesopores are not involved in the transport. Mathematically, this is expressed through introducing a boundary pore diameter, $d_{bd}^{a,c}$, for both the cathode and anode. The respective porosities and mesopore surface areas $\varepsilon_{l2}(d_{bd})$, $S_{l2}(d_{bd})$ must be subtracted from the experimental values of $\varepsilon_{l2}(d)$ and $S_{l2}(d)$ for a given value of d. The empirical correlation for hydraulic permeability

Table 1. Porous structure characteristics of titanium current collectors

Characteristic	*Porous titanium type*				
	Ti1	*Ti2*	*Ti3*	*Ti4*	*Ti5*
Specific volume ($cm^3 g^{-1}$)	0.0899	0.0924	0.0526	0.1952	0.0647
Specific surface ($m^2 g^{-1}$)	0.5800	3.0023	0.3799	2.8794	0.0855
Mean pore diameter (μm)	17.10	2.52	7.66	52.56	24.93
Total porosity (%)	28.25	22.73	18.99	42.71	21.95
Breakdown pressure (atm)	0.14	1.00	0.30	0.01	0.17

then takes the form

$$K_{l2} = \frac{[\varepsilon_{l2}(d) - \varepsilon_{l2}(d_{bd})]^3}{11[S_{l2}(d) - S_{l2}(d_{bd})]^2}, \quad K_{g2} = \frac{(\varepsilon_{g2})^3}{11(S_{g2})^2} \quad (11)$$

The 'liquid' and 'gaseous' porosities and surface areas make up the respective total porosity and total surface area as

$$\varepsilon_{l2} + \varepsilon_{g2} = \varepsilon_2, \quad S_{l2} + S_{g2} = S_2$$

The value of d_{bd} was taken as 0.0272 μm for Ti2 and Ti4 collectors, and as 0.2 μm for Ti3 and Ti5 collectors. The variation of d_{bd} within the 'forbidden' diameter range was presumed not to affect the results. The Ti1 collector exhibits a specific three-peak pattern in the differential distribution curve (Fig. 3), which makes the determination of transport pore boundary uncertain. Given 0.0272 μm as a possible diameter, another optional value of d_{bd}, according to the program may be taken as 0.2 μm. These two values determine the total porosity for diameters $d > d_{bd}$. Simultaneously, the inner surface areas of these pores differ by about 10% for different values of d_{bd}. However, this difference using the two values is not too great and is, presumably, within the accuracy of the model.

At present, no reliable experimental data on the structure of electrocatalyst layers are available. For example, the properties of disperse platinum were shown to vary depending on the method of preparation [8]. We have used a powdered sample of platinum black for our model studies. The specific volume and inner surface for mesopores with diameter $6.4 \leqslant d \leqslant 800$ nm were measured on a Sorptomatic-1900 (Carlo Erba) volumetric adsorption instrument using water adsorption and low-temperature krypton or nitrogen absorption methods. The experimental results have shown $\varepsilon_{l1} = 0$ and $S_{l1} = 0$ for $d < 6.4$ nm. The specific volume for mesopores was 0.096 716 $cm^3 g^{-1}$, and for macropores with $d > 800$ nm it was 0.034 $cm^3 g^{-1}$. The measured specific surface of 11.661 $m^2 g^{-1}$ refers to the mesopores only, since the adsorption method is of little use for measuring the macropore distribution characteristics. In our model, the macropore diameters were presumed to be uniformly distributed within the range $800 < d < 2000$ nm. For this range, the 'liquid' porosity, as a function of the diameter (in metres), takes the form

$$\varepsilon_{l1} = \varepsilon_{lme} + \varepsilon_{lma}\frac{d - 8 \times 10^{-7}}{2 \times 10^{-6} - 8 \times 10^{-7}} \quad (12)$$

where ε_{lme} and ε_{lma} are the partial meso and macroporosities. Accordingly, the total porosity is $\varepsilon_l = \varepsilon_{lme} + \varepsilon_{lma}$. The hydraulic permeabilities were calculated from Equation 10 or Equation 11 without specifying a transport pore boundary, since the distribution was unimodal. The gas breakdown pressure was taken as $\bar{P}_{br}^{a,c} = 2$ atm (the bar over the symbol P indicates that the pressure is expressed in atmospheres).

4. Cell voltage drop

Formulae for estimating the voltage drop U across the cell are now developed. Equation 13 was derived in a conventional manner [9] from the electrochemical potentials μ_{H_2}, μ_{O_2}, μ_{H_2O}, μ_{H^+}, μ_e for an electrolysis cell under equilibrium conditions at the membrane boundary:

$$U = U^{\emptyset} + \frac{RT}{4F}\ln\{[\bar{P}_g^c(D)]^2[\bar{P}_g^a(D)]\} + \phi^a(D) + \phi^c(D) + \frac{1}{F}[\mu_{H^+}^a(D) - \mu_{H^+}^c(D)] \quad (13)$$

Applying the laws of non-equilibrium thermodynamics to the H^+-ion exchange membrane and regarding the current density J and the pressure difference $P_l^a(D) - P_l^c(D)$ as the driving force for the transport of water molecules and protons, gives

$$\frac{1}{F}[\mu_{H^+}^a(D) - \mu_{H^+}^c(D)] = \frac{Jl_m}{\kappa_m} + \frac{n}{FC_0}[P_l^c(D) - P_l^a(D)] \quad (14)$$

Equation 14 takes into account, in the voltage balance, the ohmic losses across the membrane with conductivity κ_m and the streaming potential, which may be ignored, in practical calculations. The first two terms in Equation 13 are thermodynamic in nature; $\phi^a(D)$ and $\phi^c(D)$ are the reaction overpotentials.

Using the chemical potentials as estimated by standard heat capacities and ignoring the dependence of μ_{H_2O} on pressure, the standard water decomposition voltage $U^{\emptyset}$ as a function of temperature is obtained as

$$U^{\emptyset} = \frac{1}{2F}\left[295.3 \times 10^3 - 194.7T + 31.76T\ln\left(\frac{T}{298.15}\right)\right] \quad (15)$$

At a temperature of 30° C, Relationship 15 yields $U^{\phi} = 1.225\,\text{V}$.

When analysing the relationships for the overpotentials, the simplifying assumption that the electrochemical reaction within the catalyst layer proceeds in an ohmic-activation regime with simple kinetic function is made

$$i^{a,c} = 2i_0^{a,c}\,\text{sh}\left(\frac{1}{2}\frac{F\phi^{a,c}}{RT}\right) \tag{16}$$

where i is the reaction current per effective unit area of catalyst and i_0 is the exchange current. It has been stated above (in discussing the filtration equations) that the depth of the reaction zone is significantly smaller than the catalyst layer thickness. Then, assuming $x' = l_1^a + l_2^a - x$, by Ohm's law the anodic layer overpotential may be written

$$\kappa_0^a \frac{d^2\phi^a}{dx^2} = S_{11}^a(D)i^a \tag{17}$$

under the boundary conditions $\kappa_0^a d\phi^a/dx' = -J$ at $x' = 0$ and $\phi^a = 0$ at $x' = \infty$. The same applies to the cathodic layer, with x replaced by y, and x' by y'. Integrating Equations 16 and 17 with respect to the variables ϕ and $d\phi/dx$ and assuming that the electric resistance across the layer is accounted for by a factor of $\varepsilon_{11}(D)/3$, the following formula results:

$$\phi^{a,c}(D) = \frac{2RT}{F}$$

$$\times \ln\{[1 + \tfrac{1}{8}(A^{a,c})^2] + \sqrt{[1 + \tfrac{1}{8}(A^{a,c})^2]^2 - i}\}$$

where

$$A^{a,c} = \sqrt{\frac{3F}{RT}}\,J/\sqrt{\kappa_0^{a,c}S_{11}^{a,c}(D)\varepsilon_{11}^{a,c}(D)i_0^{a,c}}$$

Finally, for the temperature dependence of κ_m, the formula

$$\kappa_m(T) = \kappa_m(303.15)\exp\left[\frac{E}{R}\left(\frac{1}{303.15} - \frac{1}{T}\right)\right] \tag{18}$$

may be suggested, with the activation energy $E \approx 21\,\text{kJ mol}^{-1}$.

5. Computational results and discussion

In the computations, the parameters for the water electrolysis SPE® cell shown in Table 2 were adopted. The saturated vapour pressure against temperature relationship used was as reported in [10]. The hydraulic parameters and current–voltage characteristics of the SPE® cell model were computed for the current density range 1 to $15\,\text{kA m}^{-2}$ at temperatures of 30, 60, 90° C and generated gas pressures of 1, 4, 6, 30 atm. Two versions for the cell performance – anode feed and cathode feed – have been considered.

For reduction of space, details of the computation are omitted. For both the anode and cathode feed, the mass exchange properties of the porous collectors follow the decreasing order of efficiency

$$\text{Ti5} \simeq \text{Ti3} > \text{Ti1} > \text{Ti4} > \text{Ti2}.$$

Table 2. Values of parameters used

Cell element thickness	$l_1^a = l_1^c = 20\,\mu\text{m}$ $l_2^a = l_2^c = 1\,\text{mm}$ $l_m = 240\,\mu\text{m}$
Membrane conductance at 30° C (303.15 K)	$\kappa_m = 4\,\Omega^{-1}\,\text{m}^{-1}$
Catalyst pore solution conductance	$\kappa_0^a = \kappa_0^c = 10^{-3}\,\Omega^{-1}\,\text{m}^{-1}$
Exchange current density (Equation 16)	$i_0^a = i_0^c = 10\,\text{A m}^{-2}$
Electroosmotic transport number	$n = 2$
Hydraulic membrane permeability	$K_m = 10^{-12}\,\text{Pa}^{-1}\,\text{m s}^{-1}$
Gas viscosity	$\eta_g = 1.5 \times 10^{-5}\,\text{Pa s}$
Liquid viscosity	$\eta_l = 1.0 \times 10^{-3}\,\text{Pa s}$
Surface tension coefficient at gas-liquid interface	$\sigma = 0.07\,\text{N m}^{-1}$
Current collector parameters	See Table 1 and Figs 2 and 3

Typical computational results are presented in Tables 3 and 4. The significant drop in moisture content across the collector thickness is noteworthy: at high current density, the electrolyte depletion occurs on the inner side B, whereas the moisture content on the outer side A is presumed to be constant, corresponding to the equilibrium breakdown pressure P_{br2}. This takes place when the mass flux of reactant water tends to a maximum feasible under the given conditions. In contrast, the less vigorous convective motion due to the concentration gradient in a porous medium with a reacting solute [11] does not cause a higher moisture gradient. The type Ti3 collectors with small (about 1 μm) pore diameter, and small specific surface, provide for a higher mass-exchange rate and are, therefore, preferred. The employment of Ti2 collectors (with large specific surface of small pores) can cause electrolyte depletion at high current densities and, consequently, the interruption of electrolysis.

In observing the moisture content as a function of increasing current density, it is seen that at first the collector zone (region B; see Tables 3 and 4) and then the reaction zone (region D; see Tables 3 and 4) become depleted of electrolyte. Such a behaviour was especially characteristic of the type Ti2 collector. At a pressure of 1 atm under the anodic feed conditions, the current density of $5\,\text{kA m}^{-2}$ was a critical one, with the anode collector moisture content (anodic region B) dropping down to 5%. Further increase in current density made the anode collector 'dry up' almost completely. This resulted in a sharp voltage jump up to 4.47 V. A different picture was observed with the type Ti3 collector. An appreciable anode collector depletion was recorded at a current density of $15\,\text{kA m}^{-2}$ at least (Table 3, anodic region B, $\bar{P} =$ 1 atm). Despite the high density of current, no voltage jump was observable. Nonetheless, the voltage rose to 2.75 V. A plausible explanation is that the moisture content within the catalyst layer was sufficiently high, reaching 65% in both the anodic and cathodic regions.

The rise in generated gas pressure promotes water

*Table 3. Computed results for type Ti3 current collector (60° C)**

$\bar{P}^a = \bar{P}^c$/atm		J/kA m^{-2}	U/V	*Moisture content (fraction of maximum flooding)*				*Generated gas pressure (atm)*	
				Anode D	*Cathode D*	*Anode B*	*Cathode B*	*Anode/Cathode D/D*	*Anode/Cathode B/B*
Anodic water feed									
1	1		1.72	0.77	0.75	0.48	0.47	3.99/4.48	1.53/1.69
	5		2.21	0.70	0.69	0.31	0.41	5.12/6.44	1.90/2.35
	10		2.52	0.68	0.67	0.21	0.43	5.88/7.97	2.09/2.97
	15		2.75	0.65	0.65	0.18	0.44	6.40/9.15	2.23/3.52
30	1		1.71	0.83	0.82	0.55	0.57	32.2/32.4	30.3/30.3
	5		2.20	0.79	0.77	0.54	0.61	32.6/33.3	30.4/30.5
	10		2.50	0.76	0.75	0.53	0.62	33.0/34.0	30.4/30.6
	15		2.74	0.74	0.73	0.51	0.63	33.1/34.6	30.5/30.8
Cathodic water feed									
1	1		1.73	0.68	0.74	0.025	0.445	1.75/4.40	1.03/1.67
	5		2.25	0.406	0.674	0.015	0.093	1.60/5.41	1.15/2.04
	6		2.49	0.152	0.179	0.015	0.015	1.27/2.22	1.16/2.07
	7		2.80	0.043	0.054	0.0081	0.0091	1.10/2.12	1.09/2.09
	8		†	0.000	0.000	10^{-9}	0.0007	1.00/2.10	1.00/2.10
30	1		1.72	0.705	0.818	0.0247	0.544	30.0/32.4	30.0/30.3
	5		2.24	0.415	0.764	0.0154	0.521	30.0/33.0	30.0/30.4
	10		2.56	0.332	0.736	0.0152	0.469	30.0/33.4	30.0/30.5
	15		2.81	0.267	0.715	0.0152	0.425	30.0/33.7	30.0/30.5

* See text for details
† Not determined because of complete depletion at least of one active layer

transport to the reaction zone, since in this case the required flow rate is maintained at a lower pressure gradient across the porous elements. This manifests itself in the increased moisture content for all porous components of the electrolytic cell, which finally leads to improved performance characteristics. For the anode-fed Ti3 collector at a current density of 15 kA m^{-2}, the anodic collector moisture content was observed to increase nearly three-fold to reach 51% as the generated gas pressure rose from 1 to 30 atm. A similar effect was also recorded in the type Ti2 collector, however, with a significantly lower increase in moisture content.

The temperature rise from 30 to 90° C produced various effects on the cell performance. According to Equation 18, the increase in temperature is expected to reduce ohmic losses in the IEM. On the other hand, the calculation results have provided evidence for a greater role of reaction overpotential, owing to the increased evaporation and catalyst layer depletion.

*Table 4. Computed results for type Ti2 current collector (60° C)**

$\bar{P}^a = \bar{P}^c$/atm		J/kA m^{-2}	U/V	*Moisture content (fraction of maximum flooding)*				*Generated gas pressure (atm)*	
				Anode D	*Cathode D*	*Anode B*	*Cathode B*	*Anode/Cathode D/D*	*Anode/Cathode B/B*
Anodic water feed									
1	1		1.73	0.70	0.75	0.06	0.29	3.03/5.17	2.64/3.28
	5		2.40	0.18	0.20	0.05	0.05	3.50/4.31	3.47/4.24
	10		2.85	0.07	0.09	0.04	0.04	4.13/5.40	4.12/5.37
	15		4.47	0.001	0.001	0.000	0.003	4.34/5.61	4.43/5.61
30	1		1.71	0.84	0.82	0.39	0.62	32.3/33.0	31.1/31.6
	5		2.23	0.46	0.77	0.06	0.44	31.3/33.9	31.3/32.0
	10		2.71	0.15	0.20	0.05	0.05	31.4/31.6	31.4/31.6
	15		3.01	0.07	0.10	0.04	0.04	31.5/31.8	31.5/31.8
Cathodic water feed									
1	1		1.90	0.209	0.215	0.05	0.051	1.54/2.82	1.52/2.79
	2		2.35	0.050	0.050	0.033	0.034	1.65/3.15	1.64/3.15
	3		†	0.000	0.000	0.000	0.000	1.00/3.24	1.00/3.24
30	1		1.77	0.476	0.51	0.59	0.59	30.0/31.2	30.0/31.2
	2		2.13	0.154	0.162	0.048	0.048	30.0/31.2	30.0/31.2
	3		2.56	0.030	0.036	0.029	0.031	30.0/31.2	30.0/31.2
	4		†	0.000	0.000	0.000	0.000	30.0/31.2	30.0/31.2

* See text for details
† Not determined because of complete depletion at least of one active layer

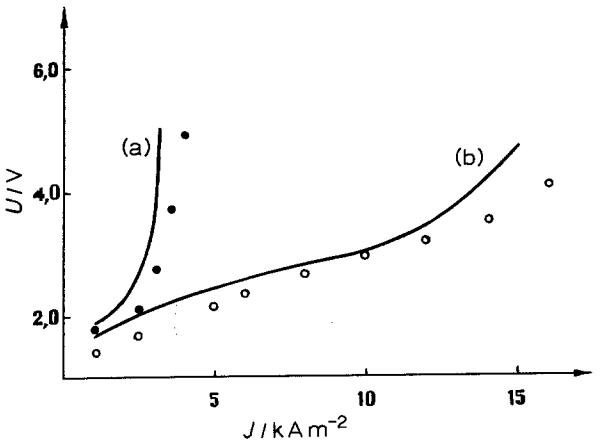

Fig. 4. Current–voltage characteristics of an SPE® cell with Ti2 type current collectors (30°C, 1 atm). (——) Computed curves; (a) cathodic feed, (b) anodic feed. Experimental values: (●) Cathodic feed, (○) anodic feed.

Quantitatively, the latter effect is determined by the porous structure of both collector and catalyst.

The macroscopic effects as modelled for the cathodic feed regime are similar to those in the above anode feed case. The only distinction is that in the former case an essential factor is the moisture content in the cathodic porous elements (cathodic regions B and D) considering that the water flux enters these structures first on its way further to the IEM and then towards the anode. An additional resistance to the process is that the water flux across the IEM is opposed to the electric current, that is, to the electroosmotic flux. Preliminary experiments have shown that this places a limit on the working current density, decreased two to three times (depending on the electrolytic cell design) in comparison to the anodic feed conditions. Simultaneously, the current reaches a limiting value which may be different for collectors with different porous structure (Figs 4 and 5). As seen in Figs 4 and 5, the

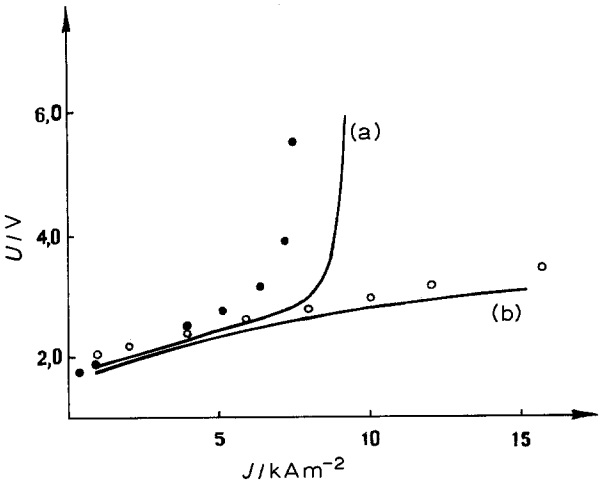

Fig. 5. Current–voltage characteristics of an SPE® cell with Ti3 type current collectors (30°C, 1 atm). (——) Computed curves; (a) cathodic feed, (b) anodic feed. Experimental values: (●) cathodic feed, (○) anodic feed.

computed curves compare satisfactorily with the experimental measurements. A discrepancy between the experimental and computational results was to be anticipated, since the model has been developed from general theoretical concepts and no attempt has been made to refine it with any fitting procedure. A number of initial parameters require further refinement and substantiation (for example, structural parameters of porous catalysts, electrochemical constants, electroosmotic transport number, porous element thickness). Finally, a percolation effect due to the breakdown of liquid phase continuity at low moisture content may be envisaged [6]. Presumably, this will lead to a limiting current lower in value as compared to that predictable by the model. However, the discussion of this issue is beyond the scope of the present work.

The data in Tables 3 and 4 show the internal gas pressure in the porous cell elements to be always higher than the manometric pressure at the cell outlet. It has been assumed in the model computations that the total of generated gas is immediately evolved into the gaseous phase. However, owing to the oversaturation of solution with the electrochemical reaction products, a certain amount of generated gas can dissolve in water and later escape into the gas phase at the rear side of the collectors. With this taken into consideration, the internal pressure is expected to decrease accordingly. The mechanism of this effect is as yet poorly understood and further experimental and theoretical studies are needed to give a full account of it.

Nonetheless, with allowance made for these inadequacies, the present model provides a satisfactory description of major kinetic effects in the performance of a water electrolysis SPE® cell. Thus, on the basis of the model developed, a better choice of energetic and macrokinetic parameters for water electrolysis technology may be suggested. Of special concern here are the characteristics of the porous SPE® electrolyser elements and the mode of water supply to the cell.

References

[1] USA Patent No. 4 546 010 (1985).
[2] L. I. Kheifets and A. B. Goldberg, *Elektrokhimiya* **25** (1989) 3.
[3] 'Synthetic Membranes: Science, Engineering and Applications, Proceedings of the NATO Advanced Study Institute) (edited by P. M. Bungay, H. K. Lonsdale and M. N. Pinko), D. Reidel, Dordrecht (1986) 733 pp.
[4] U. M. Vol'fkovich, N. V. Kuleshov, and E. L. Philippov, *Elektrokhimiya* **16** (1980) 1512.
[5] L. I. Kheifets and A. B. Goldberg, *Teor. Osnovy Khim. Tekhnol. (TOKhT)* **16** (1982) 627.
[6] L. I. Kheifets and A. V. Neimark, 'Mnogofaznye protsessy v poristykh sredakh' ('Multiphase processes in porous media'), *Khimiya*, Moscow (1982) 320 pp.
[7] R. B. McMullin and G. A. Muccini, *AIChE Journal* **9** (1956) 393.
[8] A. A. Vedenyapin, A. Yu. Krylova, A. G. Gazaryan, T. I. Kuznetsova, O. A. Malykh, G. I. Emel'yanova, A. L. Lapidus, and S. V. Yushin, *Elektrokhimiya* **27** (1991) 848.
[9] J. S. Newman, 'Electrochemical Systems', Prentice Hall, Englewood Cliffs, NJ (1973) 432 pp.
[10] R. B. McMullin, *J. Electrochem. Soc.* **116** (1969) 416.
[11] L. M. Pisman, *Chem. Eng. Sci.* **31** (1976) 693.